Electrochemical Imaging of Thermochemical Catalysis

Xiangdong Xu[1], William C. Howland[2], Daniel Martín-Yerga[1,3], Cole Cadaram[2], Deiaa M. Harraz[2], Geoff D. West[4], Patrick R. Unwin[1]*, Yogesh Surendranath[2]*

[1]Department of Chemistry, University of Warwick, Coventry CV4 7AL, U.K.

[2]Department of Chemistry, Massachusetts Institute of Technology, Cambridge, Massachusetts 02139, United States.

[3]Department of Chemistry, Nanoscience Center, University of Jyväskylä, Jyväskylä 40014, Finland.

[4]Warwick Manufacturing Group, University of Warwick, Coventry CV4 7AL, U.K.

Abstract: Thermochemical redox catalysis is critical to a wide array of key chemical transformations and is known to be sensitive to catalyst surface structure. Yet there exist limited operando tools for quantitatively imaging heterogeneities in catalytic rate across a surface. Since many thermochemical redox reactions can proceed via the coupling of electrochemical half-reactions, electrochemical microscopies can, in principle, be used to image heterogeneities in thermochemical redox catalysis. Herein, we develop a methodology for imaging variations in the rate of thermochemical redox catalysis using electrochemical microscopy. Using Pt-catalyzed aerobic oxidation of formic acid oxidation as a test reaction, scanning electrochemical cell microscopy (SECCM) imaging reveals grain-dependent variations in catalytic rate for the underlying oxygen reduction and formic acid oxidation half-reactions, implying inter-grain cooperativity during ensemble thermochemical catalysis via lateral current flows that galvanically couple disparate active sites. Tafel analysis of current-potential profiles in the presence of both reactants reveals the nature of cross-talk between the two half-reactions and provides quantitative spatially-resolved images of catalytic rates for the net thermochemical reaction. These studies establish a methodology for using electrochemical microscopy to image thermochemical catalysis and expose how electrochemical half-reactions couple and interact across surface structures to enable redox transformations.

Thermochemical redox catalysis is critical across the chemical value chain with applications ranging from the generation of small molecule energy carriers to the synthesis of value-added fine chemicals. In particular, redox catalysis underpins modern synthetic methods for functional group interconversion and cross-couplings that simultaneously increase reaction scopes and improve atom economy.[1-6] Additionally, hydrogenation and oxidation reactions of key energy relevant molecules, including N_2, CO_2, O_2, lignin, and sugars are essential for the sustainable synthesis of fuels and commodity chemicals.[7-13] Metal surfaces are excellent catalysts for a wide variety of these thermochemical redox reactions. However, our understanding of heterogeneous redox catalysis remains limited, in part, because of the heterogeneity of active sites on display at most metal surfaces. Thus, strategies for mapping catalytic activity for these reactions across a surface would advance fundamental understanding, and potentially enable the rational design of tailored heterogeneous redox catalysts with enhanced performance.

Extensive investigations have focused on achieving spatially-resolved operando measurements of heterogeneous catalytic systems. A variety of techniques have been developed depending upon the length scale of interest.[14] Magnetic resonance imaging (MRI) methods provide insight into the impact of mass transfer phenomena on product accumulation and inhomogeneity of reaction selectivities on the scale of reactors.[15,16] Observation of inhomogeneities on a nanometer to micrometer length scale, necessary for discrimination of active sites and chemical microenvironments, has generally been pursued with various forms of microscopy. Electron microscopy techniques such as high-resolution transmission electron microscopy (HRTEM) and photoemission electron microscopy (PEEM) can report on the state of the catalyst surface on these length scales.[17] HRTEM provides the capability to observe changes to catalyst morphology under realistic reaction conditions.[17,18] PEEM provides information about surface speciation, but is only practical under near-vacuum conditions.[17,19] While these electron microscopy techniques provide invaluable information about catalyst structure and adsorbate populations, they provide little direct spatially-resolved insight into local catalytic rates. Instead, strategies for resolving spatial inhomogeneities in thermocatalytic reaction rate has relied primarily on confocal optical microscopies (IR, UV-vis, and fluorescence).[14,20-23] These techniques, which image spectroscopic signatures of products or on-cycle reaction intermediates, provide rich information about rate heterogeneities, particularly for photocatalytic reactions.[20,24] However, these techniques are restricted to those reactions for which kinetically relevant spectroscopic signatures exist natively or can be introduced with minimal perturbation. Additionally, the diffusion of spectroscopic reporters on the catalyst surface or in solution must be taken into account in this analysis.[20] The enormous insights offered by these spatially-resolved catalytic microscopies motivate the development of new imaging methodologies that leverage orthogonal and complementary modes for quantifying local catalytic rates.

Recent work has shown that a diverse collection of heterogeneously catalyzed thermochemical redox reactions proceed by electrochemical band-mediated half-reaction mechanisms.[25-31] In such mechanisms, the net thermochemical reaction consists of opposing electrochemical half-reactions that may be independently investigated as electrolytic processes using voltammetric techniques. The growing understanding of the role of electrochemical processes in thermochemical redox catalysis raises the tantalizing prospect of using spatially-resolved electrochemical microscopy techniques to image variations in catalytic activity for a thermochemical transformation.

Since current flow can be quantified with excellent sensitivity, electrochemical microscopy can be used to measure reaction rates across small areas of exposed catalyst with sub-micrometer dimensions. In particular, scanning electrochemical cell microscopy (SECCM) uses an electrolyte-filled pipette to confine the reaction area to the footprint of a contacting droplet bridging the pipette tip and the surface;[32-34] meniscus contact is made to an array of different locations to image electrochemical activity across a catalyst surface. The spatial resolution of the technique is limited primarily by the size of the pipette (typically 30 nm to 2 μm), and imaging from 50 nm[35] to a few μm[36] resolution has been demonstrated.

Herein, we develop a workflow and methodology (Figure 1) for imaging thermochemical redox catalysis using electrochemical microscopy. We use SECCM to image grain-dependent catalytic activity on polycrystalline Pt for the aerobic oxidation of formic acid. This reaction is known to proceed via the coupling of the electrochemical oxygen reduction (ORR) and formic acid oxidation

(FAOR) half-reactions.[25] As both half-reactions are known to occur with different activity on a wide variety of Pt surface terminations, this reaction provides a stringent test case for the application of this imaging methodology.[37-39] We collect electrochemical activity images for each half-reaction in isolation and then corresponding images of catalytic activity when both co-reactants are present. Activity maps of the individual half-reactions in isolation provide initial estimates of the distribution of mixed potentials across the surface during the overall reaction and imply the existence of microscopic lateral current fluxes across the catalyst surface that galvanically couple disparate sites during thermochemical catalysis. Tafel analysis of current-potential profiles in the presence of both reactants provides spatially-resolved images of catalytic rate. This analysis also exposes the nature of cross-talk between the two half-reactions at short-range length scales. Cross-talk refers to the influence that one reactant has on the opposite half-reaction when both reactants, FA and O_2, are present. Specifically, the presence of O_2 enhanced the FAOR, while the presence of FA inhibited the ORR. This work establishes a methodology for using electrochemical microscopy to image thermochemical catalysis and provides rich insights into how electrochemical half-reactions couple and interact across surface structures to enable thermochemical redox transformations.

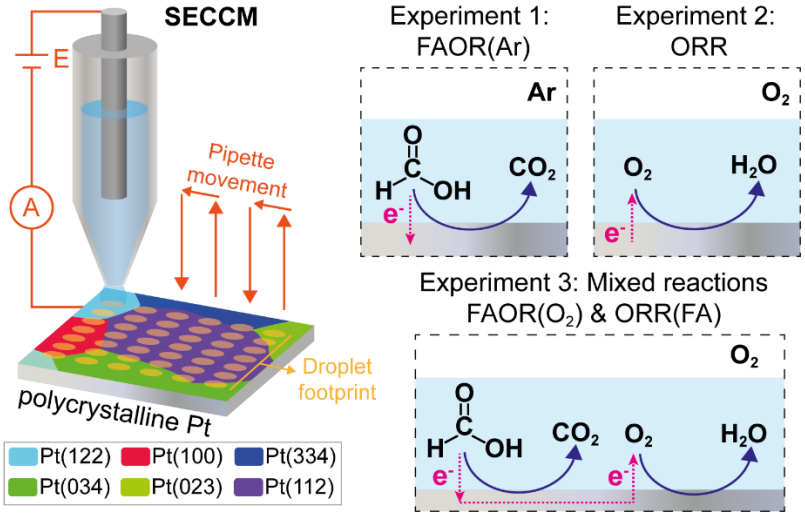

Figure 1. *Schematic of the SECCM methodology to study each half-reaction in isolation (experiment 1 and 2) and with both reactions together in the same region of a polycrystalline Pt surface (experiment 3). Each yellow spot on the Pt surface represents the droplet footprint left by SECCM meniscus contact in each individual measurement. The red arrows indicate the movement of SECCM pipette from spot to spot across the surface of Pt.*

Results and Discussion

Isolated FAOR and ORR half-reactions show grain-dependent electrocatalytic activity

As illustrated in Figure 1, we initially employed SECCM to image surface heterogeneity for each half-reaction in isolation: the FAOR under an Ar atmosphere in the absence of O_2, denoted as FAOR(Ar); and the ORR in the absence of FA. To elucidate the effect of surface structure, e.g., crystallographic orientations, on electrochemical reactions, we employed identical-location electron

backscatter diffraction (EBSD). This technique allowed us to characterize the crystallographic structure of the Pt surface, which exhibited eight different grains within the probed region (Figure 2a) with orientation distributions close to (122), (344), (334), (023), (100), (112), (034) and (144) planes. Notably, the Pt(112) plane consisted of three adjacent grains, all oriented close to this plane as shown in Figure S1. Therefore, we analyzed these three grains as a single Pt(112) grain although we acknowledge that there are small differences in surface structure. We subjected the Pt sample to UV and electrochemical cleaning for 300 cycles before each experiment. Figure S2 shows the voltammetric response obtained during the electrochemical cleaning process, with the resulting voltammograms being consistent with a clean polycrystalline Pt surface (hydrogen adsorption and desorption peaks as main indicators).[40] After rinsing with deionized water and drying with nitrogen gas, we carried out subsequent SECCM measurements on the same 340×340 μm^2 region.

To study the FAOR(Ar), we performed SECCM using a deaerated solution of 0.5 M FA in 0.1 M $HClO_4$, with the cell under a continuous Ar gas flow, by recording linear sweep voltammetry (LSV) from 0.10 to 1.05 V at a scan rate of 1 V s^{-1} at 1156 positions across the selected area. Leveraging the sensitive current response (at the pA level) of SECCM and the conical diffusion regime imposed by the pipette geometry ensures minimal iR drop and rapid mass transport.[41] These features permit high voltametric scan rates, which allows access to a large number of measurements at practical timescales. A Ag/AgCl wire reference electrode was used for SECCM experiments (see Methods), and all potentials discussed herein are reported relative to the reversible hydrogen electrode (RHE). The grains of interest spanned sizes from tens to hundreds of micrometers (Figure 2a). This size range required a 10 µm lateral separation between each SECCM meniscus landing spot to ensure a broad representation of surface grains within a single experiment. We recorded individual LSVs at each position on the surface, which are rendered as equipotential spatially-resolved maps (34x34 pixels) of current density as a function of potential (SI, Movie S1). The experiment left footprints derived from the drying of individual SECCM droplet residues as depicted in Figure S3a, with an average diameter of ca. 1.4 µm (Figure S3b). This footprint demarcates the probed area, which was used to calculate the current density. Surface roughness is found to be relatively uniform across all Pt crystal facets and equal to approximately 4 nm (Figure S4).

A qualitative evaluation of the spatially-resolved equipotential frame captured at 0.69 V (Figure 2b, derived from Movie S1) reveals grain-dependent FAOR(Ar) activity. This heterogeneity is also visualized from average voltammograms (Figure 2c) of the eight different grains. To quantitatively assess activity variations, the electrochemical data from each grain is extracted and represented as a distribution of current densities at 0.69 V (Figure S3c), which also reflects the surface heterogeneities within individual grains. We observed average current densities as high as 0.66 ± 0.02 mA cm^{-2} in the Pt(144) grain (yellow in Figure 2b) and in some regions of Pt(112), which exhibited 0.61 ± 0.04 mA cm^{-2}. In contrast, current densities as low as 0.36 ± 0.03 mA cm^{-2} were observed for Pt(100). Within each grain, current density distributions showed some heterogeneity (standard deviations of 0.02-0.04 mA cm^{-2}) that can be attributed to the subtle surface structural variations within grains. Through an inverse pole figure representation (Figure S3d), we noted a general trend where grains with orientations closer to (100) were less active for FAOR(Ar). This observation aligns with previous single crystal measurements where Pt(100) was unreactive unless pre-treated with oxygen, whereas both Pt(111) and Pt(110) readily catalyze the FA decomposition.[42]

To study the ORR half-reaction, we performed a SECCM experiment using a 0.1 M $HClO_4$ solution under a continuous O_2 gas flow, and recorded LSVs from 1.04 to 0.42 V vs RHE at a scan rate of 1 V s^{-1} over the same selected area (Figure 2a and Figure S5a), applying the same cleaning procedure. The dynamic spatially-resolved response is represented as a sequence of current density maps as a function of potential (SI, Movie S2). The average diameter of the footprints was ca. 1.3 µm in this case (Figure S5b). The equipotential map captured at 0.69 V (Figure 2d) along with the average voltammograms (Figure 2e) display the heterogeneous grain-dependent ORR activities. The distribution of current densities at 0.69 V (Figure S5c) reveals that grains with orientations close to (100) and (112) exhibit superior ORR activity (0.62 ± 0.03 mA cm^{-2} and 0.59 ± 0.04 mA cm^{-2}, respectively), while Pt(023) is the less active (0.44 ± 0.02 mA cm^{-2}) among the eight grain orientations. The inverse pole figure (Figure S5d) shows that grain orientations with contributions from (111) and (100) exhibited higher activity compared to those with contributions from (110) and (100), a finding that aligns with previous SECCM measurements.[39]

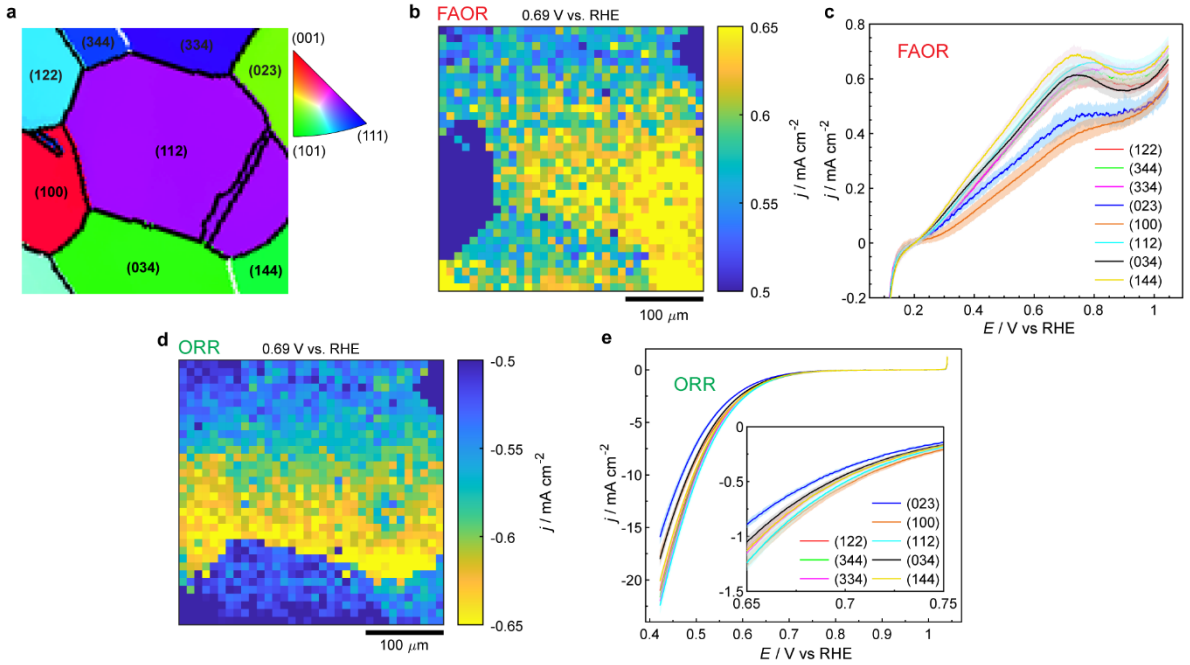

***Figure 2**. a) EBSD grain orientation map of the polycrystalline Pt surface probed during the SECCM experiments. b) Spatially-resolved equipotential snapshot of FAOR(Ar) obtained by SECCM (Movie S1) at a potential of 0.69 V using 0.5 M FA in 0.1 M $HClO_4$ under a continuous Ar flow. c) Average voltammograms of eight grains obtained from the FAOR(Ar) measurement. d) Spatially-resolved equipotential snapshot of ORR obtained by SECCM (Movie S2) at a potential of 0.69 V using 0.1 M $HClO_4$ under a continuous O_2 flow. e) Average voltammograms of eight grains obtained from the ORR measurement. Inset shows the magnified voltammograms in the potential window of 0.65 – 0.75 V. Scan rates for the LSV curves were 1 V s^{-1}.*

Mixed potential theory analysis suggests inter-grain cooperativity during thermochemical catalysis

Mixed potential theory has been demonstrated to accurately describe the correlation between an overall thermocatalytic aerobic oxidation and its constituent electrochemical half-reactions for carbon-supported metal nanoparticle catalysts.[25] Within this framework, coupled catalytic active sites operate as a short-circuited electrochemical cell, where both half-reactions occur, generating an equal yet opposite current flux that is maintained at a steady-state mixed potential.[25,26] Our previous research confirmed the validity of this short-circuit model and specifically showed that for carbon-supported Pt nanoparticles,[25] the mixed potential and reaction rate is well predicted by simply overlaying the current-potential curves for each individual half-reaction. Importantly, in these prior studies, the conductive carbon support affords facile electrochemical coupling of half reactions occurring on disparate particles and the Pt nanoparticles themselves feature a diversity of facets and surface defects capable of electrochemical coupling with each other. Consequently, these prior studies obscure the nuances of electrochemical coupling on short length-scales localized to a single surface termination. In order to unpack this complexity, we first apply mixed potential theory to the electrochemical measurements of each half-reaction in isolation to arrive at a prediction of the rate and mixed potential during thermochemical catalysis and then compare these predictions to the measured values of mixed potential and rate in the presence of both reactants in the following sections.

Figure 3a illustrates that by overlaying the LSV transients from representative SECCM pixels of FAOR(Ar) and ORR, after the capacitive current correction (with a negligible value of 0.02 ± 0.06 mA cm^{-2} for FAOR(Ar) and 0.06 ± 0.004 mA cm^{-2} for ORR, respectively), a predicted current equivalency point (E_{LSV}) can be obtained, where the current densities of the independent half-reactions are equal in magnitude, but opposite in sign. In the limit that the half-reactions operate entirely independently of each with no cross-talk, this E_{LSV} values should match the open circuit potential during thermochemical catalysts. This assumption is rigorously evaluated in the following sections, but we first examine the surface heterogeneity of this predicted mixed potential. Applying this analysis to all the corresponding SECCM pixels of FAOR(Ar) and ORR reveals grain-dependent behavior, as shown in Figure 3b-3c. From the grain-average values (blue line, Figure S6a), an E_{LSV} as high as 718 ± 6 mV is observed for grain (100), while the lowest value (682 ± 3 mV) is observed for grain (144). Through the exchange current from the individual half-reactions (j_{0_half}) map (Figure 3d) and the grain-average j_{0_half} (red line, Figure S6a), we can derive a prediction of the grain-dependent reaction rate for the FA thermochemical catalytic oxidation in the limit that the half-reactions operate independently. The results show that Pt(100) provides the lowest j_{0_half} (0.38 ± 0.03 mA cm^{-2}), with Pt(023) being the second lowest (0.43 ± 0.04 mA cm^{-2}), suggesting that these orientations are less active for the thermochemical oxidation. Meanwhile, Pt(112) and Pt(144) are the most active grain orientations (0.61 ± 0.04 and 0.65 ± 0.02 mA cm^{-2}, respectively). Interestingly, the current equivalency points do not vary significantly within the three Pt(112) grains with an average value of 690 ± 3 mV despite subtle surface structure variations as previously discussed, but the j_{0_half} analysis exhibits more heterogeneities across these grains, suggesting that the catalytic activity is more sensitive to surface structure variations than the mixed potential. The inverse pole figures (Figure S6b-S6c) show that grains with greater contribution from Pt(100) generally exhibit a more positive E_{LSV} and lower j_{0_half}. Importantly, the average value (691 ± 10 mV) of E_{LSV} from all the SECCM measurements (Figure 3b) is close to the corresponding E_{LSV} value of 0.75 V measured for ensemble-averaged carbon-supported Pt nanoparticles.[25]

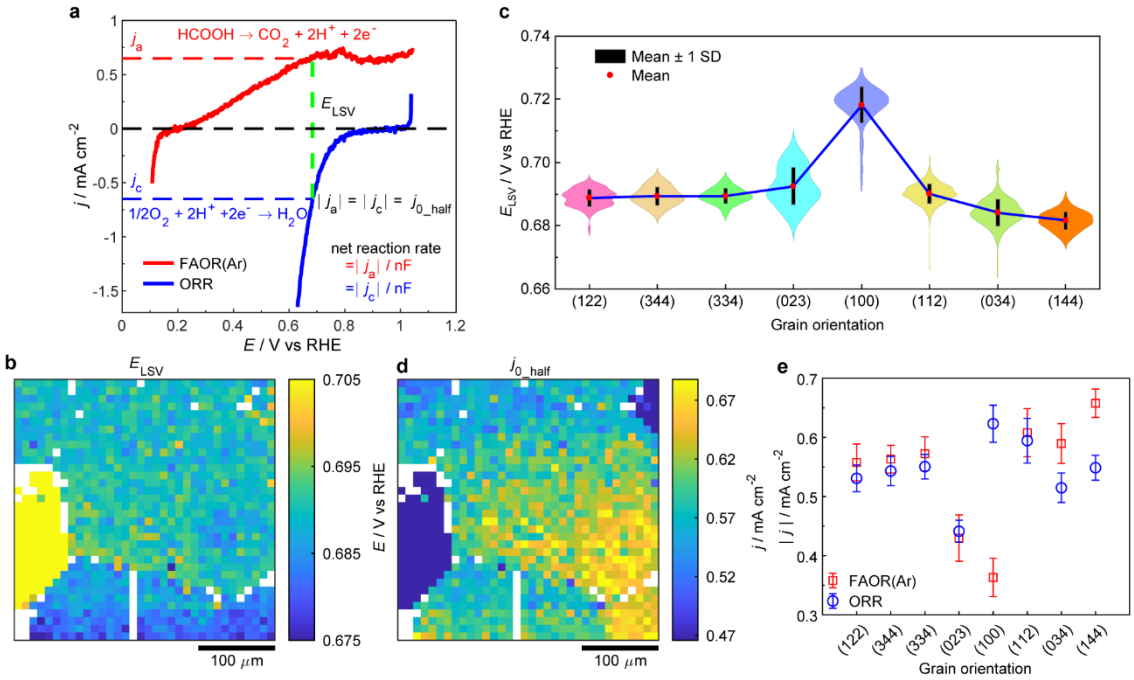

Figure 3. *a) Representative LSV traces of isolated FAOR(Ar) and ORR illustrating the calculation of the current equivalency potential (E_{LSV}) and the exchange current density (j_{0_half}), where the absolute current densities of both reactions are equal. b) E_{LSV} map produced from all SECCM spots, based on the mentioned calculation. c) The violin plot of E_{LSV} on the eight different Pt grains probed during the SECCM experiments. d) j_{0_half} map at E_{LSV} produced from all SECCM spots. Note that some pixels in these maps where left blank white to account for a small lateral shift between corresponding pixels for the two independent SECCM experiments, particularly to avoid mismatch in pixels close to grain boundaries. e) Grain-average surface current density (absolute value) at 0.69 V for FAOR(Ar) and ORR.*

The differences in E_{LSV} for the different regions of the catalyst are reflective of the differences in relative activity toward the two half-reactions and imply cooperativity between regions of the catalyst when they are exposed to a shared electrolyte medium. Comparing the spatially-resolved equipotential frames at 0.69 V for both FAOR(Ar) (Figure 2b) and ORR (Figure 2d) reveals significant variations (Figure 3e) in relative activity between the two half-reactions from grain to grain. The potential of 0.69 V is chosen because it is the average predicted mixed potential (Figure 3b-3c). For many of the grains with orientations close to (122), (344), (334), (023) and (112), we observe similar average current densities at 0.69 V towards FAOR(Ar) and ORR, with a maximum difference of 5% (Table S1). However, FAOR(Ar) than ORR activities diverge for other grains. For example, grains close to (034) and (144) show about 14.5% and 19.9% higher current density towards FAOR(Ar) than ORR, respectively. The most substantial reactivity difference is observed on Pt(100), which is more active for ORR than FAOR(Ar), displaying ca. 42% higher average current density towards ORR than FAOR(Ar).

Considering these findings from a thermochemical catalysis perspective, wherein the catalyst surface acts as a unified assembly of distinct grains, our results imply an interplay between different microscale active sites for the FAOR(Ar) and the coupled ORR across the full ensemble of surface

terminations. This interplay implies the existence of lateral charge flow across the most active sites, creating a galvanic coupling between different regions. Regions of different orientations will form short-circuited electrochemical cells with one another. To achieve the uniform potential required by the electrical and ionic conductivity of the system, regions with relatively positive isolated mixed potentials will be driven to become cathodes and regions with relatively negative isolated mixed potentials will be driven to become anodes. Because each region is thus driven to carry out in excess the reaction for which it is relatively more active, this phenomenon is cooperative in nature and may lead to greater overall thermochemical activity for the ensemble than for each isolated grain. This analysis also challenges the commonplace notion in thermochemical heterogeneous catalysis that a singular facet or site is the most active for a given reaction and suggests instead that the coupling of disparate sites and facets may furnish the highest reaction rates.

Analysis of concurrent half-reactions reveals images of local mixed potential and catalytic rate

To study how the surface structure affects the measured mixed potential and catalytic rate, we carried out an SECCM experiment using 0.5 M FA in 0.1 M $HClO_4$ under a continuous O_2 gas flow over the same area as previous experiments. In this case, the voltametric sweep was from 0.40 to 1.14 V vs RHE at a scan rate of 1 V s^{-1}. This large potential range captures regions at low potentials where the observed current is dominated by ORR even while in the presence of formic acid, ORR(FA), and regions at positive potential where the observed current is dominated by FAOR even while in the presence of O_2, FAOR(O_2). At intermediate potentials, the observed current is the sum of countervailing contributions from ORR(FA) and FAOR(O_2). These different regions can be observed from the average voltammograms (Figure 4a) of eight different grains, and the spatially-resolved maps for ORR(FA) taken at 0.50 V (Figure 4a, green circle) and FAOR(O_2) taken at 0.69 V (Figure 4a, red star) are displayed in Figure 4b and 4c, respectively. The spatially-resolved electrochemical movie is represented in Movie S3, and examples of the footprints left by the SECCM experiment (ca. 1.4 µm) are shown in Figure S7a-S7b. These activity maps reveal that strong grain-dependent activity variations persist even when both reactants are present in the media. As observed above for FAOR(Ar) and ORR recorded independently, many of grains display comparable activity for ORR(FA) as well as FAOR(O_2) leading to the similarity in the overall map in Figure 4b and 4c.

The zero crossing of the voltametric traces provides a direct measurement of the mixed potential, E_{mixed}, at which FAOR(O_2) and ORR(FA) display equal and opposite current densities, resulting in a net current of zero. To analyze the grain-dependence of E_{mixed} across the Pt surface, we extracted the E_{mixed} in each SECCM pixel to create a spatially-resolved map (Figure 4d). The distribution of (Figure 4e) and grain-averaged (blue line in Figure S7c, and Figure S7d) E_{mixed} values show more positive values on Pt(023) and Pt(100), 590 ± 3 mV, and a lower E_{mixed} (584 ± 3 mV) was observed on Pt(112). We note that the mean E_{mixed} values fall in the range of 584 to 590 mV, which is approximately ~0.1 V lower than the range of E_{LSV} values predicted from electrochemical data of each half-reaction in isolation – this topic is discussed in detail below. Notwithstanding, the differences in E_{mixed} across the probed surface are relatively small, with a maximum average difference of 6 mV. This is a direct reflection of the fact that for most grains, high FAOR(O_2) activity also coincides to high ORR(FA) activity, as seen in Figure 4b and 4c. Thus, while an increased rate of FAOR(O_2) for a given grain will push E_{mixed} to lower values, this is compensated for on most grains by a coincident acceleration in the rate of ORR(FA) that pushes E_{mixed} to lower values. The compensation between the two effects

lead to E_{mixed} values that are relatively similar across grains. Nonetheless, we stress that given the metallic conductivity of the support the short length-scales separating grains, these small variations in E_{mixed} are more than ample to drive lateral current flows between grains, or between hot spots on any given grain. Additionally, the ability to quantify these small variations in E_{mixed} highlights the sensitivity of this technique for catalytic imaging.

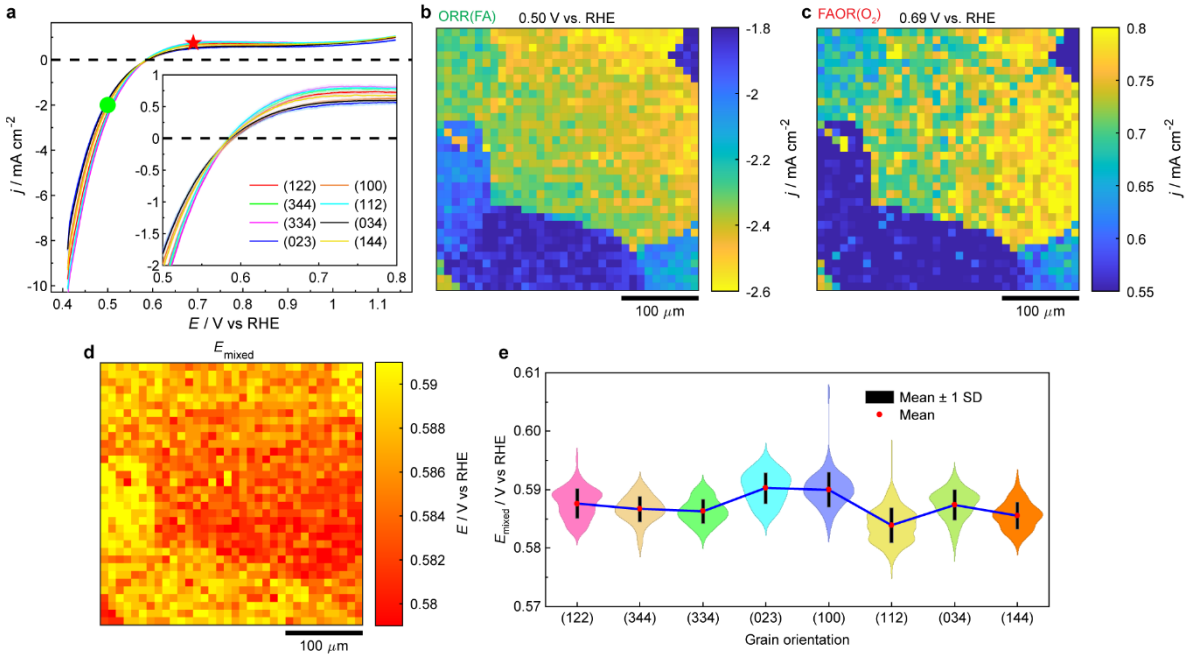

Figure 4. *a) Average voltammograms of the eight different Pt grains obtained from the SECCM measurement using 0.5 M FA in 0.1 M $HClO_4$ under a continuous O_2 flow. Scan rate was 1 V s^{-1}. Spatially-resolved equipotential snapshots obtained by SECCM (Movie S3) at potentials of b) 0.50 and c) 0.69 V, corresponding to the locations marked by green circle and red star in Figure 4a, respectively. d) Spatially-resolved mixed potential (E_{mixed}) map, built using the potential value where the net current equals zero. e) Violin plot of E_{mixed} for the eight different Pt grains probed by SECCM.*

At the mixed potential, E_{mixed}, the net current is zero, but the thermochemical catalytic rate can, none-the-less, be estimated by linearly fitting the voltametric data positive and negative of E_{mixed}. This same method of Tafel analysis was recently applied to analyze aggregate catalytic activity of Pd/C and Au/C catalysts.[43] This Tafel analysis is graphically illustrated in Figure 5a. The linear fit of the ORR(FA)-dominated curve negative of mixed potential is shown in Figure 5a, green dashed line, and the linear fit of the FAOR(O_2)-dominated curve positive of the mixed potential is shown in Figure 5a, red dashed line. These two linear fits intersect with each other at E_{Tafel}, to furnish, j_{0_Tafel}, a direct estimate of the cross-current flowing between the two half-reactions during overall thermochemical catalysis. In the limit that the Tafel regions of the fit are reflective of the kinetics of the half-reactions at the mixed potential, the intersection point E_{Tafel} should match E_{mixed} and indeed, we observe that these two values match to within 1-4 mV across all the spots investigated (Figure S8). This correspondence further supports the validity of this analysis. Accounting for the electron stoichiometry and Faraday's constant, these cross-currents directly correspond to the local catalytic rate of thermochemical FA oxidation catalysis. The spatially-resolved map (Figure 5b) and

distributions (Figure 5c) of j_{0_Tafel} clearly reveal the grain-dependent variation in thermochemical reaction rates. The ORR(FA) Tafel slopes across all spots in 0.44-0.54 V potential range are shown in Figure S9a, and the FAOR(O_2) Tafel slope in 0.66-0.76 V potential range is shown in Figure S9b. By calculating the average j_{0_Tafel} (red line in Figure S7c, and Figure S7e) as a function of grain orientations, we observe that Pt(023), Pt(100) and Pt(034) show relatively low j_{0_Tafel} (0.36 ± 0.05, 0.37 ± 0.03 and 0.38 ± 0.04 mA cm^{-2}, respectively). In contrast, Pt(334) displays a relatively high activity (j_{0_Tafel} of 0.56 ± 0.05 mA cm^{-2}). The variability in activity observed among different grains during simultaneously occuring half-reactions demonstrates that even if the current flow required to galvanically couple both electrochemical half-reactions is confined to short distances within individual grains, there will nonetheless be spatial heterogeneity in local reaction rates for the thermochemical FA oxidation across the catalyst surface. These measurements of local catalytic activity are inherently indirect because it is difficult, if not impossible, to directly quantify product formation by conventional methods (e.g. gas chromatography) on this lengthscale, given the small amount of product generated within each spot. However, the average SECCM-inferred catalytic rate across the eight distinct grains, 0.48 ± 0.09 mA cm^{-2}, is in line with the specific rate of thermochemical FA oxidation, 0.35 ± 0.04 mA cm^{-2}, measured independently by gas chromatography quantification of the produced CO_2 from polycrystalline Pt supported on a polytetrafluoroethylene gas diffusion electrode (Pt/PTFE GDE) under the same reaction conditions (Figure S10, see supporting information for measurement details). This agreement is remarkable given the ~10^9-fold smaller catalyst surface area sampled in each SECCM spot relative to the macroscopic Pt/PTFE GDE. Thus, albeit indirect, this analysis provides among the highest resolution maps of local activity for a thermochemical catalytic reaction, highlighting the power of this electrochemical imaging methodology.

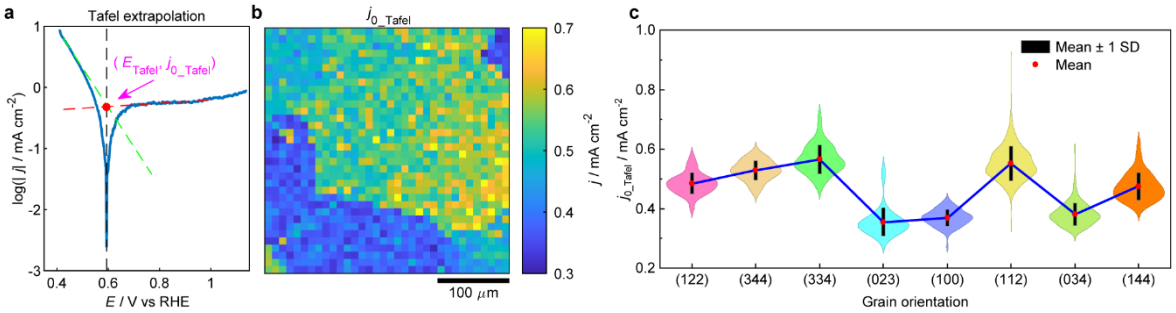

Figure 5. *a) Representative voltammogram in Tafel representation (log|j|-E plot) used for calculating the exchange current density (j_{0_Tafel}) for the ORR (with presence of FA) and the FAOR (with presence of O_2). b) SECCM spatially-resolved map and c) grain-dependent violin plot of j_{0_Tafel} calculated from the Tafel analysis.*

Comparative analysis between isolated and concurrent half-reactions reveals the origin of cross-talk between co-reactants

The above studies allowed us to determine the current equivalency potential (E_{LSV}) derived from analysis of each independent half-reaction in isolation, and the measured mixed potential (E_{mixed}) derived from the zero current potential when both reactions take place simultaneously. In the limit that the two half-reactions are entirely independent of each other, the E_{LSV} should match the E_{mixed} during the net thermochemical FAOR (purple dashed parity line, Figure 6a). However, the data

presented in Figures 6a-6b indicate a deviation from the predicted values, with the measured E_{mixed} (~0.6 V) systematically lower than the predicted E_{LSV} (~0.7 V) values by ~0.1 V. This observation implies that when the reaction is confined to the small length-scales and singular metal facets probed here, the presence of O_2 perturbs the electrokinetic profile of electrochemical FA oxidation and/or vice versa. This effect is defined as cross-talk between the co-reactants and the independent half-reactions, i.e., O_2 influences the FAOR and FA affects the ORR. This perturbation is also reflected in deviations, albeit to a smaller extent, between the exchange current density j_{0_half} and j_{0_Tafel} (Figure S11) for many of the grains.

To further investigate the origin of the above discrepancy, we compared the aggregate voltammetric profile when both reactants are present (Figure 6c, blue) with the voltammetric profile of FAOR(Ar) (Figure 6c, red) and ORR (Figure 6c, green) in isolation. The potential of zero current in Figure 6c, blue provides E_{mixed} and the overlay of these traces, provides a measure of the expected current density for isolated ORR (Figure 6c, pink dot on green line) and FAOR(Ar) (Figure 6c, pink dot on red line) at E_{mixed}. These expected current densities can be compared to the measured rate of catalysis, j_{0_Tafel}, from the above Tafel analysis. This analysis reveals that the average j_{0_Tafel} for FAOR(O_2) is slightly higher than the current density at E_{mixed} for the FAOR(Ar) in most grains (blue vs red data, Figure 6d), although the absolute differences are small, ranging from 0.01 to 0.11 mA cm^{-2} (Table S2). This indicates that the presence of O_2 slightly promotes the FAOR half-reaction on most grains[44] (Figure S12), likely due to the facilitated removal of adsorbed CO, a known poison for FAOR[45,46]. This analysis also reveals that, in contrast to the modest promotion of FAOR in the presence of O_2, the presence of FA substantially attenuates ORR. The average j_{0_Tafel} for ORR(FA) is 1.84 to 2.95 mA cm^{-2} (Table S2) lower than the corresponding values for ORR in isolation and this inhibition is observed across all grains (blue vs green data in Figure 6d, and Figure S12). This strong attenuation of ORR is also attributed to the generation of CO poisons that form during concurrent FAOR.[47,48] The poisoning effect of CO serves to increase the required overpotential for ORR to achieve a given rate leading to the observed negative shift of E_{mixed} relative to E_{LSV}. Notably, the negative shift of E_{mixed} relative to E_{LSV} is not observed for Pt nanoparticles supported on carbon,[25] a phenomenon that may arise from many factors including metal support interactions, distinct facets or defects present on nanoparticles, and or gradients in O_2 and/or formate within the Pt/C catalyst film. All of these effects may serve to enhance the oxidative removal of CO poisons[44,48,49] and/or to inhibit the degree of cross-talk in the first place. Notwithstanding, these findings suggest a potential benefit to spatial separating ORR and FAOR catalysis, perhaps via a mixed ion/electron conducting membrane, so as to minimize cross-talk and maximize catalytic rates.

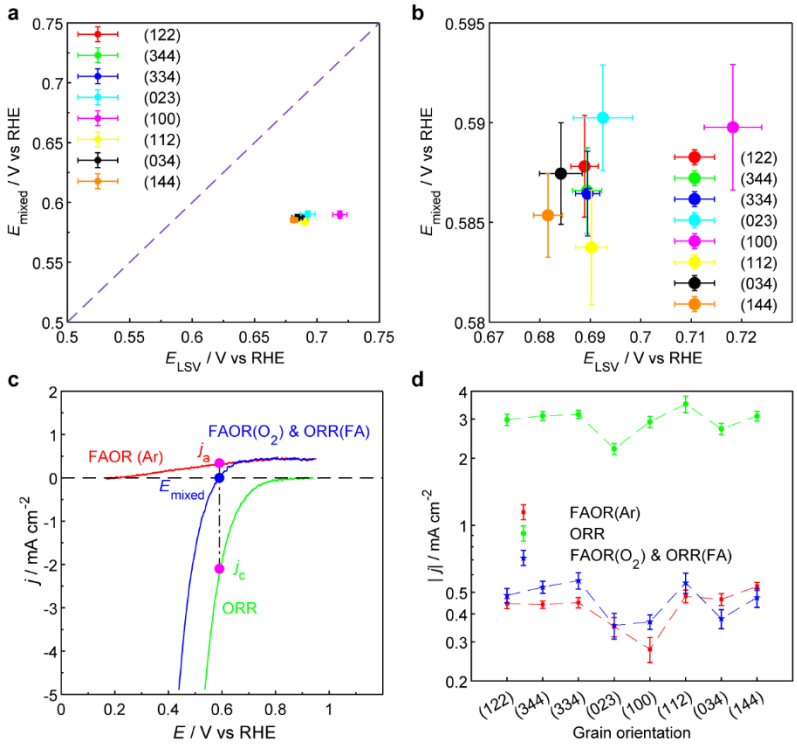

Figure 6. *a) Relationship between the average equivalent current potential (E_{LSV}) and the average mixed potential (E_{mixed}) on the eight different Pt grains probed with SECCM. Dashed line indicates perfect correspondence. b) Magnified version of the plot in (a). c) Schematic illustrating the calculation of the current density for FAOR(Ar) and ORR at measured E_{mixed}. d) Average exchange current densities for FAOR(O_2) and ORR(FA) based on Tafel analysis, and current densities extracted at E_{mixed} for FAOR(Ar) and ORR as a function of Pt grains.*

Conclusion

In this study, we demonstrate that SECCM can be employed to generate spatially-resolved images of local catalytic rates for thermochemical redox transformations that proceed via the coupling of electrochemical half-reactions. Using formic acid oxidation as a test case, we analyze the current-potential profile of oxygen reduction and formic acid oxidation in isolation and the aggregate profile in the presence of both co-reactants. Analysis of each half-reaction in isolation reveals grain-dependent variations in catalytic activity. While many grains display similarly high (or low) activity for both half-reactions, some grains, such as Pt(100) display divergent activity for each half-reaction, with high activity for ORR and low activity for FAOR(Ar). These findings challenge the notion of single most active surface site and instead imply inter-grain cooperativity during ensemble thermochemical catalysis via lateral current flows that galvanic couples grains with preferential competency for each half-reaction. Analysis of the aggregate current-potential profile in the presence of O_2 and FA reveals that strong grain-dependent activity variations persist even when the half-reactions take place concurrently and Tafel analysis provides direct images of local variations in catalytic rate with high spatial resolution. Finally, comparison of the isolated and aggregate current-

potential profile reveals the nature of cross-talk between half-reactions. The presence of FAOR serves to substantially attenuate ORR activity whereas the presence of ORR serves to modestly enhance FAOR activity, effects that are ascribed to the presence and removal of CO poisons on the catalytic surface, respectively. Overall, this study builds a bridge between electrochemical microscopy and thermochemical catalysis, and showcases how electrochemical half-reactions couple and interact across surface structures to enable redox transformations.

Methods:

Sample preparation

A platinum foil (99.95+%, Goodfellow, UK) with a thickness of 0.25 mm was manually polished using a polishing cloth (MicroCloth^{TM}, Buehler, USA) and monocrystalline diamond water-soluble sprays (Kemet, UK) of various particle sizes: 3 µm, 1 µm, 0.5 µm and 0.1 µm, respectively. After each polishing step, the Pt foil was sonicated in deionized water (18.2 MΩ.cm at 25 Cº, ELGA Labwater) for 30 min to remove any remaining diamond powder. Before being used as a working electrode, the Pt foil was annealed under a butane flame and then quickly quenched into deionized water, a process that was repeated 3 to 5 times. This step was important for cleaning surface contaminants, alleviating surface pressure, and allowing the surface to recrystallize to show clear grains and grain boundaries. Before each SECCM measurement, the Pt foil was first cleaned using an ultraviolet (UV) cleaner (Zone II for SEM, Hitachi, Japan) to eliminate hydrocarbon contamination from electron microscopy imaging. The Pt foil was then electrochemically cleaned in a standard three-electrode system, using a Pt coil as the counter electrode and a commercial leakless Ag/AgCl electrode (3.4 M KCl, LF-2-100, Innovative Instruments, Inc., USA) as the reference electrode (RE). Cyclic voltammetric measurements were performed on the Pt foil in deareated 0.1 M $HClO_4$, scanning from 0.15 V to 1.0 V, back to -0.2 V, and stopping at 0.15 V with respect to the Ag/AgCl RE. This process was repeated for 300 cycles at a scan rate of 50 mV s^{-1}. The Pt foil was then rinsed with deionized water and dried under N_2 gas flow in preparation for the local SECCM experiments. These electrochemical and UV cleaning processes did not change significantly the Pt surface structure as analyzed by EBSD (Figure S13).

Pipette, electrolyte and quasi-reference electrodes

Single-barrel pipettes with a diameter of 1 µm were prepared using a P2000 laser-based micropipette puller (Sutter Instruments, US) from borosilicate capillaries (1.2 mm outer diameter, 0.69 mm inner diameter, 100 mm length, BF120-69-10, Harvard Apparatus). An Ag wire (Goodfellow, UK) with a diameter of 0.125 mm was electrochemically oxidized within a potential window between +5 and +7 V vs. Pt counter electrode in a saturated KCl solution for 10-15 min to prepare AgCl-coated Ag quasi-reference counter electrodes (QRCEs). The Ag/AgCl QRCEs, demonstrating high stability[50], were routinely calibrated by measuring the open circuit potential with a commercial leakless Ag/AgCl electrode both before and immediately after each SECCM experiment. And then the potential was converted relative to the RHE. The SECCM pipettes were filled with different solutions depending on the process being studied: deaerated 0.5 M FA in 0.1 M $HClO_4$ for the FAOR(Ar), 0.1 M $HClO_4$ for the ORR, and 0.5 M FA in 0.1 M $HClO_4$ for the FAOR/ORR mixed processes.

SECCM experiments

SECCM experiments were conducted using a custom-built multifunctional instrument, as described previously.[33,36] The SECCM setup was placed inside a Faraday cage with heat sinks and acoustic foam to minimize electrical noise, thermal drift, and acoustic noise. The Faraday cage was placed on an optical table (RS 2000, Newport) to minimize mechanical vibrations. The system was controlled using Labview 2019 software, running the Warwick Electrochemical Scanning Probe Microscopy (WEC-SPM)[51] platform, in communication with an FPGA card (PCIe-7852R, National Instruments) for data acquisition and instrument control. The current was measured every 4 µs, and averaged 257 times (one point for data transfer), yielding a data acquisition rate of 1028 µs per data point.

The Pt foil, which served as the working electrode, was placed inside an environmental cell[52] under a continuous flow of gas (either Ar or O_2). This cell was on top of an xy-piezoelectric positioner (P-733.2, Physik Instrumente, Germany) for lateral movement. The pipette was filled with the required electrolyte, equipped with an Ag/AgCl QRCE, and then mounted on a z-piezoelectric positioner (P-753.2, Physik Instrumente, Germany). Micropositioners (M-461-XYZ-M, Newport, US) provided coarse movement in x, y, and z axes to bring the pipette close to the Pt surface. Hopping-mode SECCM was used to perform experiments on the Pt surface. The pipette initially approached the surface under a bias potential of -0.45 V, 0.50 V and -0.13 V vs the Ag/AgCl QRCE for FAOR(Ar), ORR, and mixed reactions, respectively, until the liquid meniscus at the tip of the pipette contacted the Pt surface. The surface current was monitored and used as a feedback signal to stop the vertical movement of pipette when contact is detected. Linear sweep voltammetry measurements were then carried out using different potential windows and sweep direction depending on the reaction studied. A scan rate of 1 V s^{-1} was used to access thousands of measurements across the surface at a practical timescale. After measurements at one location were finished, the pipette was retracted and moved to the next location across the Pt surface with a lateral distance of 10 µm to repeat the same measurement protocol.

Physical characterisation

The footprints left by SECCM were imaged by field emission scanning electron microscopy (FE-SEM, ZEISS Gemini, Germany) to determine the geometric surface area and calculate current densities. A JEOL 7800F with a symmetry Electron Backscatter Diffraction (EBSD, Oxford Instruments, UK) detector was used to identify the grain orientations of the identical SECCM locations. EBSD data were analysed using AztecCrystal software. The Pt topography was characterized by AFM (Park NX10) to evaluate the surface roughness (root mean square roughness, R_q).

Data analysis

All the raw data were processed with Matlab. In our analysis to predict the current equivalency point (E_{LSV}), individual SECCM pixels from different experiments were matched to correspond to near identical locations. However, achieving exact pixel-by-pixel alignment in repeated SECCM experiments is challenging, potentially resulting in minor mismatches between pixels in these studies (albeit less than 10 µm). To mitigate the effects of these discrepancies, particularly around grain

boundaries, we have excluded certain pixels from the maps (Figures 3b and 3d) and corresponding analyses. This approach ensures that all corresponding data points align with the same grain and their proximate locations for all the independent experiments. Inverse pole figures were made following a previously reported methodology.[53] Tafel analysis was performed using a Python code specifically tailored for the data in this study.[54]

Acknowledgements

We would like to acknowledge Kunal M. Lodaya, Sophia Weng, and Max J. Hülsey for their assistance with the aerobic FAOR catalytic rate measurements and Dr. James A. Gott for collecting the AFM data. X.X. and P.R.U. acknowledge financial support from the European Union's Horizon 2020 research and innovation programme under the Marie Skłodowska-Curie grant agreement no. 812398 (SENTINEL). X.X. and P.R.U. acknowledge UK's Engineering and Physical Sciences Research Council for funding under grant EP/V037943/1 (Sustainable Chemicals Innovations Enabling Net Carbon Emissions, SCIENCE). D.M.-Y. acknowledges financial support from the Research Council of Finland (ref. 355569). Y.S. acknowledges support from the Air Force Office of Scientific Research (AFOSR) under award number FA9550-20-1-0291.

References

1. Grzybowski, M., Sadowski, B., Butenschön, H. & Gryko, D. T. Synthetic Applications of Oxidative Aromatic Coupling—From Biphenols to Nanographenes. *Angew. Chem. Int. Ed.* **59**, 2998-3027 (2020). https://doi.org/10.1002/anie.201904934
2. Yang, Y., Lan, J. & You, J. Oxidative C–H/C–H Coupling Reactions between Two (Hetero)arenes. *Chem. Rev.* **117**, 8787-8863 (2017). https://doi.org/10.1021/acs.chemrev.6b00567
3. Liu, C., Liu, D. & Lei, A. Recent Advances of Transition-Metal Catalyzed Radical Oxidative Cross-Couplings. *Acc. Chem. Res.* **47**, 3459-3470 (2014). https://doi.org/10.1021/ar5002044
4. Chen, B., Wang, L. & Gao, S. Recent Advances in Aerobic Oxidation of Alcohols and Amines to Imines. *ACS Catal.* **5**, 5851-5876 (2015). https://doi.org/10.1021/acscatal.5b01479
5. Ryland, B. L. & Stahl, S. S. Practical Aerobic Oxidations of Alcohols and Amines with Homogeneous Copper/TEMPO and Related Catalyst Systems. *Angew. Chem. Int. Ed.* **53**, 8824-8838 (2014). https://doi.org/10.1002/anie.201403110
6. Yuan, Y. & Lei, A. Electrochemical Oxidative Cross-Coupling with Hydrogen Evolution Reactions. *Acc. Chem. Res.* **52**, 3309-3324 (2019). https://doi.org/10.1021/acs.accounts.9b00512
7. Bai, S.-T. *et al.* Homogeneous and heterogeneous catalysts for hydrogenation of CO_2 to methanol under mild conditions. *Chem. Soc. Rev.* **50**, 4259-4298 (2021). https://doi.org/10.1039/D0CS01331E
8. Galloway, J. N. *et al.* Transformation of the Nitrogen Cycle: Recent Trends, Questions, and Potential Solutions. *Science* **320**, 889-892 (2008). https://doi.org/10.1126/science.1136674
9. Xu, C., Paone, E., Rodríguez-Padrón, D., Luque, R. & Mauriello, F. Recent catalytic routes for the preparation and the upgrading of biomass derived furfural and 5-hydroxymethylfurfural. *Chem. Soc. Rev.* **49**, 4273-4306 (2020). https://doi.org/10.1039/D0CS00041H

10. Rosales-Calderon, O. & Arantes, V. A review on commercial-scale high-value products that can be produced alongside cellulosic ethanol. *Biotechnol. Biofuels* **12**, 240 (2019). https://doi.org/10.1186/s13068-019-1529-1
11. Sudarsanam, P., Peeters, E., Makshina, E. V., Parvulescu, V. I. & Sels, B. F. Advances in porous and nanoscale catalysts for viable biomass conversion. *Chem. Soc. Rev.* **48**, 2366-2421 (2019). https://doi.org/10.1039/C8CS00452H
12. Luo, H. *et al.* Oxidative Catalytic Fractionation of Lignocellulosic Biomass under Non-alkaline Conditions. *J. Am. Chem. Soc.* **143**, 15462-15470 (2021). https://doi.org/10.1021/jacs.1c08635
13. Ford, P. C. & Eldik, R. v. *Catalysis in Biomass Conversion*. 1st ed, Vol. 77 396 (Academic Press, 2021).
14. Weckhuysen, B. M. Chemical Imaging of Spatial Heterogeneities in Catalytic Solids at Different Length and Time Scales. *Angew. Chem. Int. Ed.* **48**, 4910-4943 (2009). https://doi.org/10.1002/anie.200900339
15. Lysova, A. A. & Koptyug, I. V. Magnetic resonance imaging methods for in situ studies in heterogeneous catalysis. *Chem. Soc. Rev.* **39**, 4585-4601 (2010). https://doi.org/10.1039/B919540H
16. Zheng, Q. *et al.* Operando magnetic resonance imaging of product distributions within the pores of catalyst pellets during Fischer–Tropsch synthesis. *Nat. Catal.* **6**, 185-195 (2023). https://doi.org/10.1038/s41929-023-00913-8
17. Rupprechter, G. Operando Surface Spectroscopy and Microscopy during Catalytic Reactions: From Clusters via Nanoparticles to Meso-Scale Aggregates. *Small* **17**, 2004289 (2021). https://doi.org/10.1002/smll.202004289
18. van der Wal, L. I., Turner, S. J. & Zečević, J. Developments and advances in in situ transmission electron microscopy for catalysis research. *Catal. Sci. Technol.* **11**, 3634-3658 (2021). https://doi.org/10.1039/D1CY00258A
19. Zeininger, J. *et al.* Pattern Formation in Catalytic H_2 Oxidation on Rh: Zooming in by Correlative Microscopy. *ACS Catal.* **12**, 11974-11983 (2022). https://doi.org/10.1021/acscatal.2c03692
20. Zhang, Y. *et al.* Superresolution fluorescence mapping of single-nanoparticle catalysts reveals spatiotemporal variations in surface reactivity. *Proc. Natl. Acad. Sci. U. S. A.* **112**, 8959-8964 (2015). https://doi.org/10.1073/pnas.1502005112
21. Ristanović, Z. *et al.* Quantitative 3D Fluorescence Imaging of Single Catalytic Turnovers Reveals Spatiotemporal Gradients in Reactivity of Zeolite H-ZSM-5 Crystals upon Steaming. *J. Am. Chem. Soc.* **137**, 6559-6568 (2015). https://doi.org/10.1021/jacs.5b01698
22. Gao, M. *et al.* Imaging spatiotemporal evolution of molecules and active sites in zeolite catalyst during methanol-to-olefins reaction. *Nat. Commun.* **11**, 3641 (2020). https://doi.org/10.1038/s41467-020-17355-6
23. van Schrojenstein Lantman, E. M., Deckert-Gaudig, T., Mank, A. J. G., Deckert, V. & Weckhuysen, B. M. Catalytic processes monitored at the nanoscale with tip-enhanced Raman spectroscopy. *Nat. Nanotechnol.* **7**, 583-586 (2012). https://doi.org/10.1038/nnano.2012.131
24. Tachikawa, T., Yamashita, S. & Majima, T. Evidence for Crystal-Face-Dependent TiO_2 Photocatalysis from Single-Molecule Imaging and Kinetic Analysis. *J. Am. Chem. Soc.* **133**, 7197-7204 (2011). https://doi.org/10.1021/ja201415j
25. Ryu, J. *et al.* Thermochemical aerobic oxidation catalysis in water can be analysed as two coupled electrochemical half-reactions. *Nat. Catal.* **4**, 742-752 (2021). https://doi.org/10.1038/s41929-021-00666-2
26. Adams, J. S., Kromer, M. L., Rodríguez-López, J. & Flaherty, D. W. Unifying Concepts in Electro- and Thermocatalysis toward Hydrogen Peroxide Production. *J. Am. Chem. Soc.* **143**, 7940-7957 (2021). https://doi.org/10.1021/jacs.0c13399

27. Huang, X. *et al.* Au–Pd separation enhances bimetallic catalysis of alcohol oxidation. *Nature* **603**, 271-275 (2022). https://doi.org/10.1038/s41586-022-04397-7
28. Howland, W. C., Gerken, J. B., Stahl, S. S. & Surendranath, Y. Thermal Hydroquinone Oxidation on Co/N-doped Carbon Proceeds by a Band-Mediated Electrochemical Mechanism. *J. Am. Chem. Soc.* **144**, 11253-11262 (2022). https://doi.org/10.1021/jacs.2c02746
29. Lodaya, K. M. *et al.* An electrochemical approach for designing thermochemical bimetallic nitrate hydrogenation catalysts. *Nat. Catal.* **7**, 262-272 (2024). https://doi.org/10.1038/s41929-023-01094-0
30. Fortunato, G. V. *et al.* Analysing the relationship between the fields of thermo- and electrocatalysis taking hydrogen peroxide as a case study. *Nat. Commun.* **13**, 1973 (2022). https://doi.org/10.1038/s41467-022-29536-6
31. Zhao, X. *et al.* Chemo-bio catalysis using carbon supports: application in H_2-driven cofactor recycling. *Chem. Sci.* **12**, 8105-8114 (2021). https://doi.org/10.1039/D1SC00295C
32. Mefford, J. T. *et al.* Correlative operando microscopy of oxygen evolution electrocatalysts. *Nature* **593**, 67-73 (2021). https://doi.org/10.1038/s41586-021-03454-x
33. Mariano, R. G. *et al.* Microstructural origin of locally enhanced CO_2 electroreduction activity on gold. *Nat. Mater.* **20**, 1000-1006 (2021). https://doi.org/10.1038/s41563-021-00958-9
34. Mariano, R. G., McKelvey, K., White, H. S. & Kanan, M. W. Selective increase in CO_2 electroreduction activity at grain-boundary surface terminations. *Science* **358**, 1187-1192 (2017). https://doi.org/10.1126/science.aao3691
35. Bentley, C. L. & Unwin, P. R. Nanoscale electrochemical movies and synchronous topographical mapping of electrocatalytic materials. *Faraday Discuss.* **210**, 365-379 (2018). https://doi.org/10.1039/C8FD00028J
36. Yule, L. C., Bentley, C. L., West, G., Shollock, B. A. & Unwin, P. R. Scanning electrochemical cell microscopy: A versatile method for highly localised corrosion related measurements on metal surfaces. *Electrochim. Acta* **298**, 80-88 (2019). https://doi.org/10.1016/j.electacta.2018.12.054
37. Subhramannia, M. & Pillai, V. K. Shape-dependent electrocatalytic activity of platinum nanostructures. *J. Mater. Chem.* **18**, 5858-5870 (2008). https://doi.org/10.1039/B811149A
38. Adzic, R. R., O'Grady, W. E. & Srinivasan, S. Oxidation of HCOOH on (100), (110) and (111) single crystal platinum electrodes. *Surf. Sci. Lett.* **94**, L191-L194 (1980). https://doi.org/10.1016/0167-2584(80)90348-5
39. Chen, C. H., Meadows, K. E., Cuharuc, A., Lai, S. C. & Unwin, P. R. High resolution mapping of oxygen reduction reaction kinetics at polycrystalline platinum electrodes. *Phys. Chem. Chem. Phys.* **16**, 18545-18552 (2014). https://doi.org/10.1039/c4cp01511h
40. van der Niet, M. J. T. C., Garcia-Araez, N., Hernández, J., Feliu, J. M. & Koper, M. T. M. Water dissociation on well-defined platinum surfaces: The electrochemical perspective. *Catal. Today* **202**, 105-113 (2013). https://doi.org/10.1016/j.cattod.2012.04.059
41. Anderson, K. L. & Edwards, M. A. Evaluating Analytical Expressions for Scanning Electrochemical Cell Microscopy (SECCM). *Anal. Chem.* **95**, 8258-8266 (2023). https://doi.org/10.1021/acs.analchem.3c00216
42. Columbia, M. R. & Thiel, P. A. The interaction of formic acid with transition metal surfaces, studied in ultrahigh vacuum. *J. Electroanal. Chem.* **369**, 1-14 (1994). https://doi.org/10.1016/0022-0728(94)87077-2
43. Kim, B. *et al.* Tafel Analysis Predicts Cooperative Redox Enhancement Effects in Thermocatalytic Alcohol Dehydrogenation. *ACS Catal.*, 8488-8493 (2024). https://doi.org/10.1021/acscatal.3c06103
44. Xu, P., Bernal-Juan, F. D. & Lefferts, L. Effect of oxygen on formic acid decomposition over Pd catalyst. *J. Catal.* **394**, 342-352 (2021). https://doi.org/10.1016/j.jcat.2020.10.032

45. Herrero, E. & Feliu, J. M. Understanding formic acid oxidation mechanism on platinum single crystal electrodes. *Curr. Opin. Electrochem.* **9**, 145-150 (2018). https://doi.org/10.1016/j.coelec.2018.03.010
46. Koper, M. T. M. Structure sensitivity and nanoscale effects in electrocatalysis. *Nanoscale* **3**, 2054-2073 (2011). https://doi.org/10.1039/C0NR00857E
47. Ustarroz, J. *et al.* Mobility and Poisoning of Mass-Selected Platinum Nanoclusters during the Oxygen Reduction Reaction. *ACS Catal.* **8**, 6775-6790 (2018). https://doi.org/10.1021/acscatal.8b00553
48. von Deak, D., Singh, D., King, J. C. & Ozkan, U. S. Use of carbon monoxide and cyanide to probe the active sites on nitrogen-doped carbon catalysts for oxygen reduction. *Appl. Catal. B: Environ.* **113-114**, 126-133 (2012). https://doi.org/10.1016/j.apcatb.2011.11.029
49. Obradović, M. D. *et al.* Formic acid oxidation on Pt–Au nanoparticles: Relation between the catalyst activity and the poisoning rate. *J. Power Sources* **197**, 72-79 (2012). https://doi.org/10.1016/j.jpowsour.2011.09.043
50. Bentley, C. L., Perry, D. & Unwin, P. R. Stability and Placement of Ag/AgCl Quasi-Reference Counter Electrodes in Confined Electrochemical Cells. *Anal. Chem.* **90**, 7700-7707 (2018). https://doi.org/10.1021/acs.analchem.8b01588
51. *Warwick Electrochemical Scanning Probe Microscopy (WEC-SPM)* <http://www.warwick.ac.uk/electrochemistry/wec-spm> (2017).
52. Ornelas, I. M., Unwin, P. R. & Bentley, C. L. High-Throughput Correlative Electrochemistry-Microscopy at a Transmission Electron Microscopy Grid Electrode. *Anal. Chem.* **91**, 14854-14859 (2019). https://doi.org/10.1021/acs.analchem.9b04028
53. Daviddi, E. *et al.* Nanoscale electrochemistry in a copper/aqueous/oil three-phase system: surface structure-activity-corrosion potential relationships. *Chem. Sci.* **12**, 3055-3069 (2020). https://doi.org/10.1039/d0sc06516a
54. Martín-Yerga, D. Tafel analysis v1.0. *Zenodo* (2023). https://doi.org/10.5281/zenodo.8177225

Graphical abstract